Supplementary Materials

Highly sensitive and robust soft tri-axial tactile sensors enabled by dual inductive sensing mechanisms

Si Chen[1], Su Li[1], Yiting Zheng[1], Brian Fong[2], Yizong Li[1], Penghao Dong[1], David Hwang[1], Shanshan Yao[1*]

[1]Department of Mechanical Engineering, Stony Brook University, Stony Brook, NY 11794, USA.

[2]Department of Electrical and Computer Engineering, Stony Brook University, Stony Brook, NY 11794, USA.

[*]**Correspondence to:** Prof. Shanshan Yao, Department of Mechanical Engineering, Stony Brook University, 161 Light Engineering, Stony Brook, NY 11794, USA.
E-mail: shanshan.yao@stonybrook.edu.

Supplementary Note 1. Comparison of reported inductive tactile sensors.

We have included a detailed comparison of various sensors, summarizing their sensing mechanisms, sensitivity, range, and materials in Supplementary Table 1. This comparison highlights the significant improvement in sensitivity—particularly in the shear direction—achieved by our sensors (Supplementary Figure 1). However, it is notable that the reported sensors have different geometries and sizes, making direct comparisons of sensing range and sensitivity across devices challenging and potentially inequitable. To address this issue, we fabricated samples with identical geometry and size, varying only the sensing mechanism (details in Supplementary Note 2). This controlled comparison ensures a fair evaluation of different inductive sensing mechanisms. The results, presented in Figure 1D, demonstrate that under these controlled conditions, our device—featuring dual-mechanism based on the Biot–Savart law and Eddy current (EC) effect, as well as a unique hybrid coil design with non-uniform line spacing and adjustable porous compressible layer (PCL)— achieves significantly enhanced sensitivity.

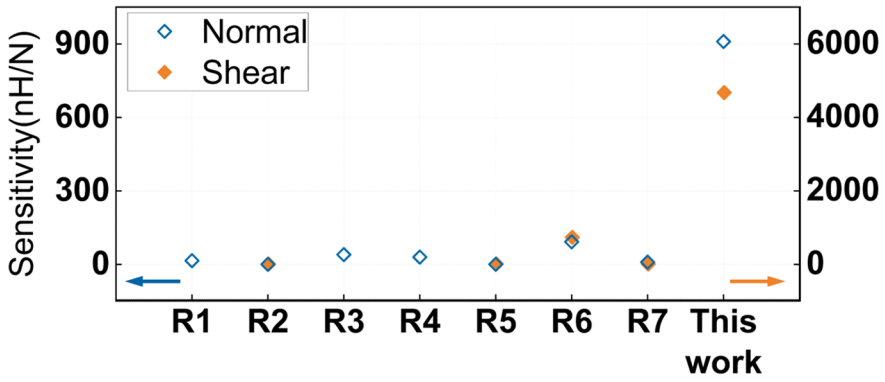

Supplementary Figure 1. Sensitivity comparison of reported inductive tactile sensors. R1-R7 represent sensors from reference[1-7].

Supplementary Table 1. Comparison of reported inductive tactile sensors.

Type	Capability	Sensitivity[1]	Range	Materials		
				Bottom Coil	Top layer	Middle layer
Magnetic film	Normal[1]	15.4 nH/N	0 – 14 N§	Rigid PCB*	Fe/Elastomer#	Ecoflex30
	Normal[2] Shear[2]	0.3 nH/N 0.9 nH/N	0 – 40 N§ 0 – 7 N§	Flexible PCB	Fe/Ecoflex30	Ecoflex30
Magnetic composite[2]	Normal[3]	40 nH/N	1 – 5 N	NiCr/Al/flexible polyimide sheet	–	Fe/Ecoflex#
Conductive target	Normal[4]	30 nH/N	0 – 15 N§	Flexible PCB	Conductive film#	Ecoflex#
	Normal[5] Shear[5]	0.4 nH/N 5 nH/N	0 – 105 N -6 – 6 N	Flexible PCB	Al	Smooth-Sil 950
	Normal[6] Shear[6]	92 nH/N 727 nH/N	0 – 13 N§ -0.7 – 0.7 N§	Flexible PCB	Al	Ecoflex20
	Normal[7] Shear[7]	9.5 nH/N 2.5 nH/N	0 – 20 N§ -2 – 2 N§	Flexible PCB	Liquid metal	Ecoflex30
This work	Normal Shear	910 nH/N 4667 nH/N	0 – 3.5 N -2.3 – 2.3 N	AgNW/PDMS	AgNW/PDMS	AgNWs embedded porous PDMS

[1] The sensitivity of different sensors is compared for the 0 − 1 N force range, where all sensors exhibit linear sensing properties.

[2] There is no top layer in inductive tactile sensors based on magnetic composites. The magnetic flux density variation is caused by the deformation of magnetic composites. Details of different mechanisms of inductive sensors can be found in Supplementary Note 2.

§ Sensing range is not provided. The data is the applied force in performance tests.

* The conductive material commonly used for PCB is copper.

Specific material information is not provided.

Supplementary Note 2. Mechanisms of different types of inductive sensors.

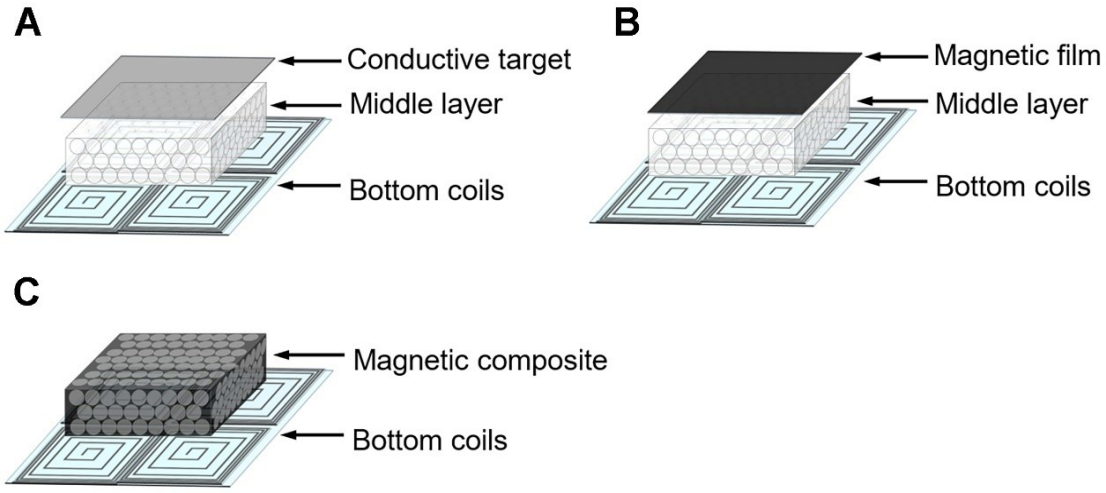

Supplementary Figure 2. Schematics of different types of inductive sensors. Inductive sensors enabled by (A) conductive target, (B) magnetic film, and (C) magnetic composite.

For the performance comparison of different inductive sensors in Figure 1D, sensors based on four different mechanisms (Supplementary Figure 2A-C and this work) were made into the same dimension, where all bottom coils were laser-patterned AgNW/PDMS coils and compressible layers (middle layer or magnetic composites) were porous Ecoflex30. The conductive target was made by printing Ag ink on a plastic substrate (Supplementary Figure 2A), the magnetic film was NdFeB/Ecoflex30 (Supplementary Figure 2B), and the porous magnetic composite was NdFeB doped porous Ecoflex30 (Supplementary Figure 2C). More details on the materials and fabrication can be found in the Experimental section in the main text.

The above inductive sensors operate based on electromagnetic induction principles. These sensors detect changes in the inductance of the bottom coils caused by variations in the magnetic field. Most inductive sensors employ the following three mechanisms for tri-axial inductive sensors, each modulating the inductance through interactions with magnetic fields in a different way.

Conductive Target (Supplementary Figure 2A): This mechanism involves a conductive top layer (i.e., the target). When approaching the bottom coils, the conductive target

induces EC that opposes the coil's magnetic field, resulting in a reduction in the coil's inductance (further explained in (Supplementary Note 3).

Magnetic Film (Supplementary Figure 2B): The top layer is a magnetic film that generates its own magnetic field, which interacts with the field from the coil. When external forces − either normal or shear − are applied, the relative position of the magnetic film and the coils is shifted, altering the magnetic interaction and the resulting inductance.

Magnetic Composite (Supplementary Figure 2C): Similar to the magnetic film interaction but the top magnetic film is replaced by a magnetic composite serving as the porous compressible medium. Here, the deformation of the magnetic composite due to external forces alters the magnetic field. This deformation further leads to changes in the inductance of the bottom coil.

Supplementary Note 3. Sensing mechanism based on the Eddy current effect.

The inductance of a conductor (L) is given by the quotient of the magnetic flux (Φ) and the current (I)

$$L = \frac{\Phi}{I} \tag{1}$$

The magnetic flux Φ through an area (A), resulting from the magnetic flux density (B), is calculated from the double integral over this area:

$$\Phi = \iint B \cdot dA \tag{2}$$

Substitute Supplementary Equation (2) into (1) leads to:

$$L = \frac{1}{I} \iint B \cdot dA \tag{3}$$

As a result, if the current is constant, L is proportional to the magnetic flux density B and the area A .

The EC effect is commonly explored as the sensing mechanism of inductive tactile sensors. Activating a coil with an alternating current (AC) generates a magnetic field that further induces ECs in nearby conductive objects.[8] As the ECs produce a magnetic field that opposes the originally generated magnetic field from the coil, the magnetic flux density within the coil reduces, and thus the inductance of the coil decreases:[4-6]

$$B_{\text{coil}} = B_{\text{AC}} - B_{\text{eddy}} \tag{4}$$

where B_{coil} is the reduced magnetic flux density of the coil, B_{AC} is the original magnetic flux density generated by the AC, and B_{eddy} is the magnetic flux density generated by the EC. If the original AC-generated magnetic flux density is kept constant, the stronger the EC, the smaller the reduced magnetic flux density.

The magnetic field generated by ECs is related to the position of the conductive target (x), the conductivity of the target (σ), the permeability of the target (μ_r), and the working frequency of the Eddy current sensor (ECS) (f),[8]

$$B_{\text{eddy}} = h\left(x, \sigma, \mu_r, f\right) \tag{5}$$

For an air core coil, $\mu_r = 1$. If the working frequency is unchanged during utilization, f is constant. When the conductive target does not fully overlap with the coil, the target position can be determined by the distance between the coil and the target (h_e), and the area of the coil covered by the target (A_e). For an ECS, B_{eddy} can be obtained as

$$B_{eddy} = g\left(h_e, \sigma, A_e\right) \tag{6}$$

According to Supplementary Equation (3), the inductance due to the original AC-generated magnetic flux density (L_{AC}) and the EC-generated magnetic flux density (L_{eddy}) are:

$$L_{AC} = \frac{1}{I}\iint B_{AC} \cdot dA \tag{7}$$

$$L_{eddy} = \frac{1}{I}\iint B_{eddy} \cdot dA_e \tag{8}$$

Substitute Supplementary Equation (6) into Equation (8):

$$L_{eddy} = \frac{1}{I}\iint g\left(h_e, \sigma, A_e\right) \cdot dA_e \tag{9}$$

$$L_{coil} = L_{AC} - L_{eddy} \tag{10}$$

As a result, for the same conductive target, the inductance of the coil (L_{coil}) is reduced by the EC. Reducing the vertical distance (Δh_e) by the normal load increases EC and reduces the inductance of the bottom coil. Conversely, reducing the lateral overlapping area (ΔA_e) decreases the EC and increases the inductance of the coil.[7]

Supplementary Note 4. Biot-Savart law and calculation of the inductance of a single-turn square coil.

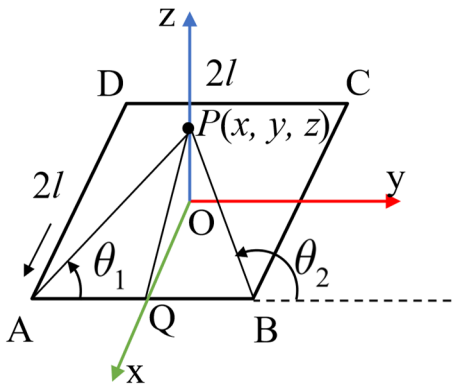

Supplementary Figure 3. Schematic of a single-turn square coil.

The inductance of a single current-carrying wire (L_{wire}) is determined by the self-inductance (L_s) and mutual inductance (L_{m}):[9]

$$L_{\text{wire}} = L_{\text{s}} + L_{\text{m}} \tag{11}$$

L_s is an inherent property of the current-carrying wire and varies with the wire's length (l) and radius (r):[10]

$$L_{\text{s}} = f(l, r) \tag{12}$$

where an increase in l and a decrease in r result in an increase in L_{s}.

L_{m} occurs when two current-carrying wires are in proximity. When these wires are placed in parallel and the currents flow in the same direction, the magnetic flux density between the wires increases.[9] Thus, their mutual inductance increases, enhancing the total inductance. Conversely, if the currents flow in the opposite direction, the magnetic flux density between the wires decreases, thereby decreasing the mutual inductance and reducing the total inductance.

A single-turn square coil (Supplementary Figure 3) can be divided into a four-segment current-carrying straight wire. The center of the square coil is the origin, and the side length

of the coil is $2l$ ($r \ll l$). According to the Biot-Savart law, a magnetic flux density ($\vec{B}$) generated by a current-carrying straight wire at the point P (x, y, z) can be calculated as[11]

$$\vec{B} = \frac{\mu_0 I}{4\pi d}(\cos\theta_1 - \cos\theta_2)\hat{u} \tag{13}$$

where d is the perpendicular distance between the point P and the wire, μ_0 is the vacuum permeability ($\mu_0 = 4\pi \times 10^{-7} N \cdot A^{-2}$), θ_1, θ_2 are angles between the two ends of the wire and the point P, I is the current carrying by the wire, $\hat{u}$ is the unit vector perpendicular to the plane defined by the segment wire and P. Therefore,

$$\overrightarrow{PA} = (x, y, z) - (l, -l, 0) = (x - l, y + l, z) \tag{14}$$

$$\overrightarrow{PB} = (x, y, z) - (l, l, 0) = (x - l, y - l, z) \tag{15}$$

$$\overrightarrow{PC} = (x, y, z) - (-l, l, 0) = (x + l, y - l, z) \tag{16}$$

$$\overrightarrow{PD} = (x, y, z) - (-l, -l, 0) = (x + l, y + l, z) \tag{17}$$

If the point P is on the z-axis, according to Supplementary Equation (13), the magnetic flux density generated by the AB-segment straight wire at the point $P(x, y, z)$ ($\overrightarrow{B_{\mathrm{AB}}}$) can be calculated as follows:

$$d = \overline{PQ} = \left|(0, 0, z) - (l, 0, 0)\right| = \sqrt{l^2 + z^2} \tag{18}$$

$$\cos\theta_1 = \cos\angle PAQ = \frac{\overline{AQ}}{\overline{AP}} = \frac{l}{\sqrt{2l^2 + z^2}} \tag{19}$$

$$\cos\theta_2 = -\cos\angle PBQ = -\frac{\overline{BQ}}{\overline{BP}} = -\frac{l}{\sqrt{2l^2 + z^2}} \tag{20}$$

$$\overrightarrow{B_{\mathrm{AB}}} = \frac{\mu_0 I}{4\pi\sqrt{l^2 + z^2}}\left[\frac{l}{\sqrt{2l^2 + z^2}} + \frac{l}{\sqrt{2l^2 + z^2}}\right] = \frac{\mu_0 I l}{2\pi\sqrt{l^2 + z^2}\cdot\sqrt{2l^2 + z^2}}\hat{u} \tag{21}$$

Due to the symmetry of the square coil, the magnetic flux densities B_{AB_x} and B_{AB_y} from opposite sides of the square coil cancel each other out.[11] This cancellation is due to the fact that the direction of magnetic flux densities produced by opposite segments are in opposite directions. Thus, only B_{AB_z} should be considered.

$$B_{\mathrm{AB}\_z} = B_{\mathrm{AB}} \cos \angle PQO \tag{22}$$

$$\cos \angle PQO = \frac{\overline{OQ}}{\overline{PQ}} = \frac{l}{\sqrt{l^2 + z^2}} \tag{23}$$

Substitute Supplementary Equation (21) and (23) into (22):

$$B_{\mathrm{AB}\_z} = \frac{\mu_0 I l^2}{2\pi\left(l^2 + z^2\right) \cdot \sqrt{2l^2 + z^2}} \tag{24}$$

Repeat this process for the other three segments of the square coil and sum up the results:

$$B_z = B_{\mathrm{AB}\_z} + B_{\mathrm{BC}\_z} + B_{\mathrm{CD}\_z} + B_{\mathrm{DA}\_z} = \frac{2\mu_0 I l^2}{\pi\left(l^2 + z^2\right) \cdot \sqrt{2l^2 + z^2}} \tag{25}$$

At the center of the single-turn square coil P (0,0,0), the magnetic flux density is

$$B_{\mathrm{single}} = \frac{\sqrt{2}\mu_0 I}{\pi l} \tag{26}$$

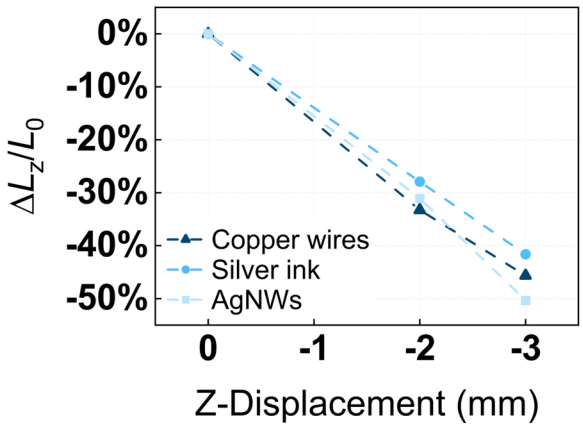

Supplementary Figure 4. Measured inductance changes along the z-axis for different materials of coils.

Supplementary Note 5. Stretchability of coils based on different conductive materials.

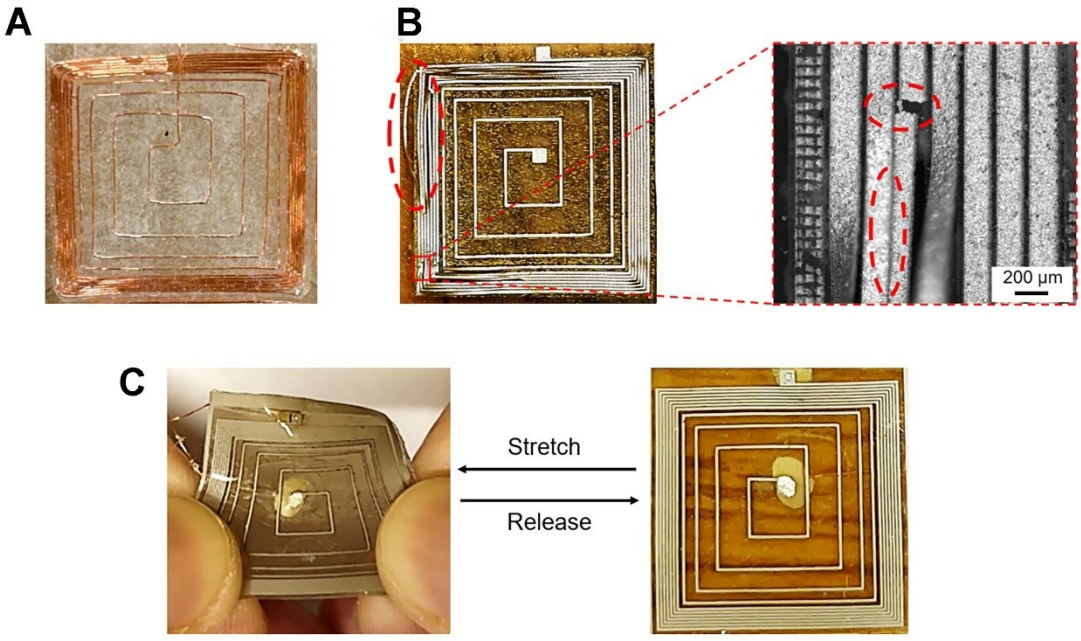

Supplementary Figure 5. Stretchability of coils based on different conductive materials: (A) copper wire, (B) silver ink, (C) AgNWs embedded in PDMS. The dashed regions in (b) show the coil damage.

The copper wire in Supplementary Figure 5A was hand-wound into a coil. It is hard to maintain a controllable line spacing and coil geometry during stretching and releasing. Silver ink was screen-printed onto a PDMS thin film (Supplementary Figure 5B). Under stretching, the silver ink tended to crack or peel off from the PDMS surface, as indicated by the red dashed regions. In comparison, coils based on AgNWs embedded in PDMS displayed good stretchability and fabrication precision. Supplementary Figure 5C demonstrates that the coils can be accurately produced through laser patterning. The coil maintained good conductivity under stretching and recovered to the original pattern upon release, indicating good mechanical robustness. Further details on the flexibility test are presented in Supplementary Figure 14.

Supplementary Note 6. Design of the hybrid multi-turn square coil.

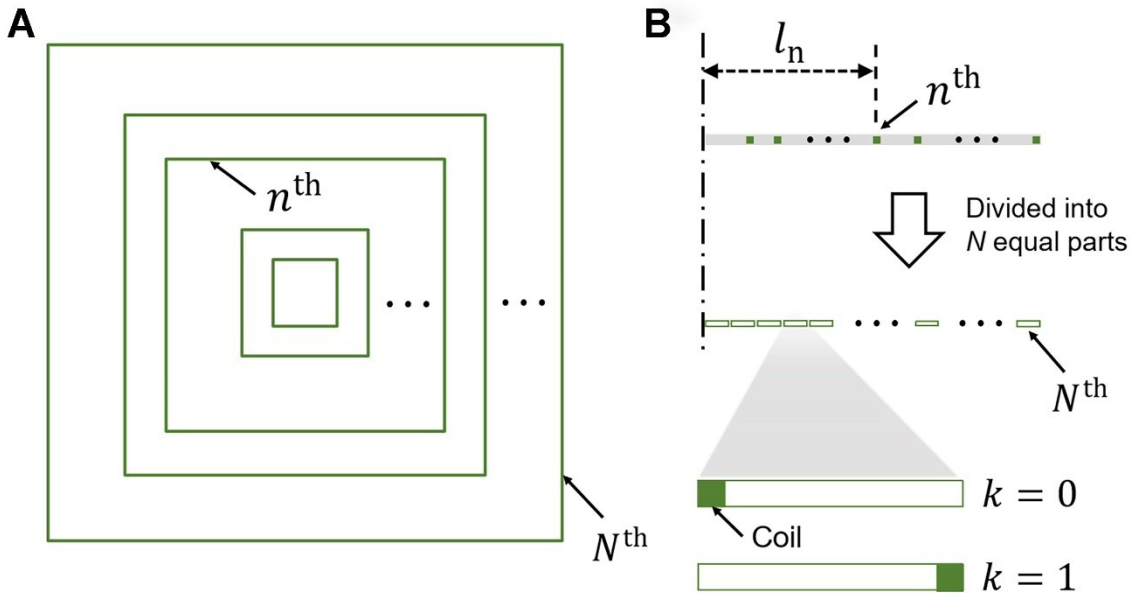

Supplementary Figure 6. Schematic illustration of the inner spiral turns of a hybrid square coil. (A) Illustration of an *N*-turn square coil with different radii. (B) The method of determining the radius for n^{th} turn of the coil. For simplicity, only the right half of an *N*-turn square coil is shown.

The coil design adopts a hybrid structure consisting of outer concentrated turns and inner spiral turns, both positioned on the same plane, as shown in Figure 4B (I).[12-14] The "concave" magnetic field distribution produced by the outer concentrated turns is effectively compensated by the "convex" magnetic field distribution from the inner planar spiral turns.[15]

For the inner spiral turns, the current distribution can be approximated using a finite number of coils that carry the same current but have different radii (Supplementary Figure 6A)[12-14]. It is assumed that an *N*-turn coil is used. The area of the original coil is divided into *N* equal segments, with each segment containing a single coil (Supplementary Figure 6B). The coefficient k ($0 \leq k \leq 1$) is used to determine the position at which the coil is placed. When $k = 0$, the coil is placed at the left end of the segment. When $k = 1$, the

coil is placed at the right end of the segment. The radius of the n^{th} coil (l_n) can be obtained as:[12-14]

$$l_n = f_n \cdot R \tag{27}$$

$$f_n = k\sqrt{1-(\frac{N-n}{N})^2} + (1-k)\sqrt{1-(\frac{N-n+1}{N})^2} \tag{28}$$

where R is the radius of the N^{th} coil.

The goal is to achieve a uniform distribution of the magnetic field across the surface of the square coil. This means that the axial magnetic flux density at any given point can be approximated the same across the entire coil surface. The central point (0, 0, 0) is then selected to calculate the magnetic flux density. From Supplementary Equation (26), the magnetic flux density generated by N turns of inner spiral turns (B_s) at the point (0, 0, 0) can be obtained as:

$$B_s = \sum_{n=1}^{N} \frac{\sqrt{2}\mu_0 I}{\pi l_n} \tag{29}$$

For the outer concentrated turns, they can be approximated as a square coil that has m concentrated turns and each turn has the same radius L_c.[12-14] Similarly, the magnetic flux density generated by the outer concentrated turns (B_c) at the point (0,0,0) can be obtained as:

$$B_c = m\frac{\sqrt{2}\mu_0 I}{\pi L_c} \tag{30}$$

From Supplementary Equations (29) and (30), the total magnetic flux density on the surface of the square coil (the same as at the point (0, 0, 0)) can be obtained as:

$$B_z = B_s + B_c = \sum_{n=1}^{N} \frac{\sqrt{2}\mu_0 I}{\pi l_n} + m\frac{\sqrt{2}\mu_0 I}{\pi L_c} \tag{31}$$

Thus, according to Supplementary Equations (27), (28) and (31), we can adjust the value of k (related to the spacing of spiral turns) and the number of turns (N and m) to ensure that the magnetic flux density of the coil is uniform and has the desired magnitude of B_z.

Supplementary Note 7. Optimization of the bottom coil.

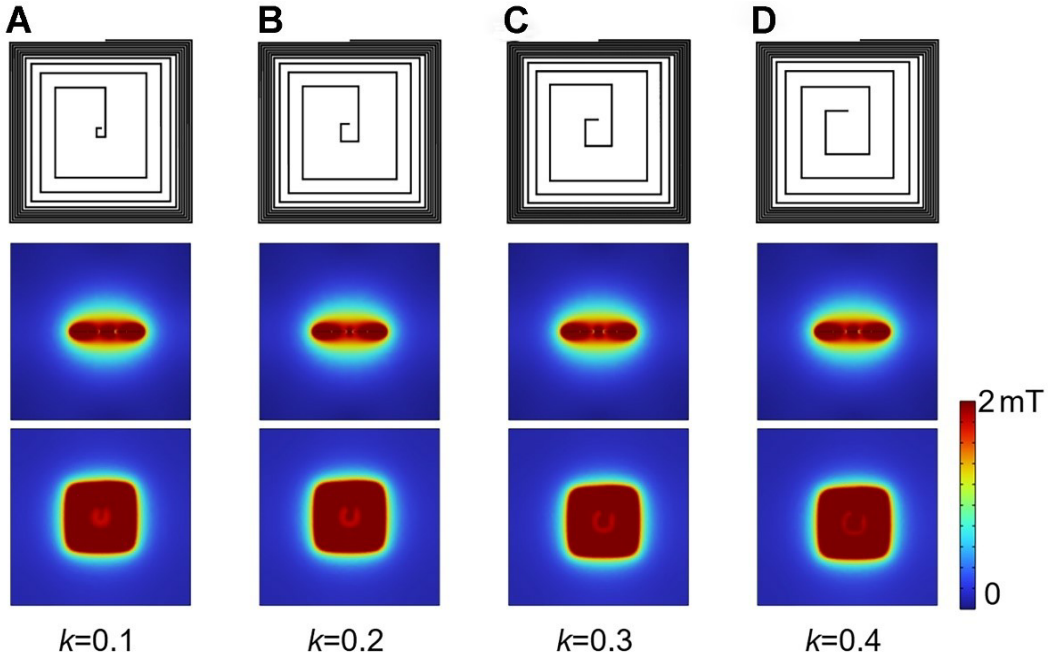

Supplementary Figure 7. Schematics of the bottom coils with varying coil parameters (top) and corresponding simulation results of magnetic flux density distributions (middle: cross-sectional view; bottom: top-view): (A) k = 0.1, (B) k = 0.2, (C) k = 0.3, (D) k = 0.4. For all bottom coils, the number of spiral turns (N) is 6 and the number of concentrated turns (m) is 5.

As discussed in Supplementary Note 6, by adjusting the value of k (related to the spacing of spiral turns) and number of turns (N for spiral turns and m for concentrated turns), the uniformity of the magnetic flux density can be achieved. To minimize the coil size, N and m are chosen to be 6 and 5, respectively. This is a well-established configuration allowing for a uniform magnetic field.[11-13] As illustrated in Supplementary Figure 7, at the inner part (close to the coil center), the uniformity of the generated magnetic flux density increases with the value of k increases. Additionally, the minimal spacing of spiral turns decreases for a larger value of k. Due to fabrication limitations, 50 μm was established as the minimal allowable line spacing. When k was increased to 0.5 and beyond, the minimal line spacing fell below 50 μm. Consequently, a k value of 0.4 was determined to be the optimal parameter for the coil to generate a uniform magnetic field.

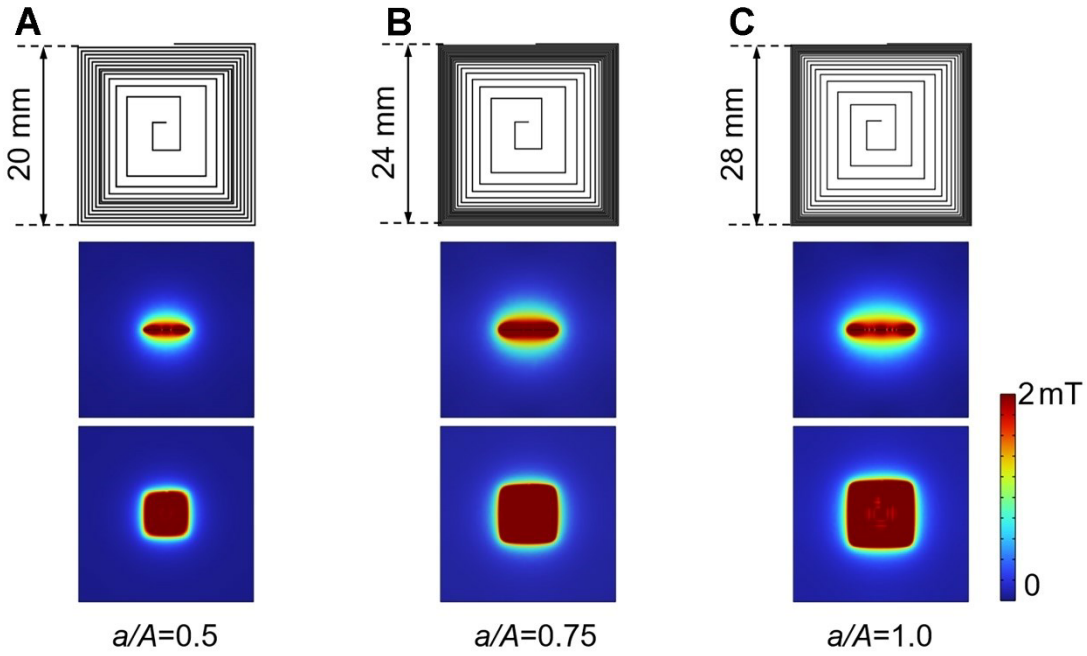

Supplementary Figure 8. Schematics of different top coil patterns with different coil sizes relative to the bottom coils (top) and corresponding simulation results of magnetic flux density distributions (middle: cross-sectional view; bottom: top-view). The optimization processes for top coils are similar to that for bottom coils. Briefly, we adjusted the number of turns (N and m) and k parameters to ensure a uniform magnetic field that matched the magnitude of the opposite magnetic field from the bottom coils.

Supplementary Note 8. Selection of laser cutting parameters

A smaller line spacing of the coil provides two primary benefits: (1) It enables a more uniform magnetic field generated by the coil (more discussion can be found in Supplementary Notes 6 and 7 and Supplementary Figure 8), and (2) it increases the coil inductance, thereby improving the stability of inductance measurements and the signal to noise ratio of the tactile sensor. For a precise coil fabrication with small line spacing, we utilized a picosecond pulsed laser source with a firing frequency of 100 kHz, a wavelength of 532 nm, and a temporal pulse width of approximately 12 picoseconds in full width half maximum. The laser source is paired with a high-speed galvanometer scanning system and a telecentric f-theta lens of 100 mm focal length for a focal spot diameter of around 20 μm diameter (1/e definition) as experimentally measured through feature size measurement for varying laser power levels.[16] Unlike continuous wave lasers, the picosecond pulsed laser minimizes the heat-affected zone on the material due to its short thermal diffusion length, resulting in minimal damage in the vicinity of laser processed region.[17-20]

The primary objective of laser patterning is to completely remove AgNW-embedded PDMS layers in the designated regions per device design and thus achieve the desired coil geometry free from circuit shorting. In the meantime, the pure PDMS layer, as a substrate, should be minimally affected to maintain the structural robustness. A laser scanning speed of 30 mm/s was chosen to induce a high pulse overlap process (around 66 laser shots per unit coil pattern length applied in this study) that has been useful for scribing relatively thick films with high precision and uniformity by scribing in a layer-by-layer fashion as an effective milling process.[18] In this work, we relied on a relatively high laser power of 1.2 W (3.82 J/cm^2 in laser fluence or energy density) to ensure device operation through perfect electrical isolation between neighboring coil patterns (Figure 3B and C) at the expense of mild damage in pure PDMS layer. Nevertheless, a narrow cutting width of around 40 μm was achieved allowing stable isolation patterning over the full device area. Detailed cutting characteristics are further visualized in the cutting cross-sectional view spatially matched with the top view (Figure 3C). It is seen that the pure PDMS layer was removed (around 45 μm depth) together with the AgNW-embedded PMDS layer (around 10 μm thickness) at the laser beam center. The region just next to the center is proven to be the taper region of

a relatively deep ablation crater in the pure PDMS layer, forming sharp cutting boundaries at the AgNW-embedded layer level ensuring complete electrical isolation – two white dotted lines marked as effective cutting boundaries, thereby showing a cutting width of around 40 μm. On the other hand, it is observed that ablated PDMS debris was redeposited near the cutting edge (and in part within ablated PDMS crater), covering the top portion of AgNW-embedded PDMS layer to the lateral extent of 40 μm from the cutting boundaries. Such a cutting edge region simply covered by the PDMS debris on top would be still part of the electrically active coil structure considering the in-plane direction of desired electric current flow, as justification of the achieved cutting width of around 40 μm (also refer to the right image of Figure 3C – part of embedded AgNWs can be seen through deposited debris near the claimed cutting edge region).

Compared to the previous work using traditional continuous laser for patterning AgNWs (with a patterning resolution of around 100 μm),[17, 21] the picosecond pulsed laser utilized in this work significantly improves patterning resolution (to around 40 μm). For the AgNW coil patterns of large interspacing, multiple two-dimensional offset laser scribing paths were used to achieve electrical isolation with a minimal processing load, resulting in grid-like patterns (left image in Figure 3C). Further studies to improve the cutting resolution with minimal PDMS damage are underway on the basis of reduced laser power and optimal laser scanning schemes (e.g., scanning speed, number of scans), and the laser parameter that can selectively remove AgNW-embedded PDMS layer only has been identified (not shown here) with little damage on the underlying pure PDMS layer, thus resulting in cutting width 20 μm or less. However, the laser patterning performance at reduced laser power levels has exhibited relatively high sensitivity to the sample preparation steps (e.g., time elapsed after the AgNW-PDMS embedding step), causing issues in achieving process uniformity over the entire device area. Therefore, ongoing efforts are in correlation with further stabilization of sample preparation steps. In this context, it is mentioned that the use of relatively high laser power in this study can accommodate possible sample variations, still tightly restricting damage in the surrounding material systems taking advantage of minimal heat diffusion in the case of picosecond pulsed laser processing.

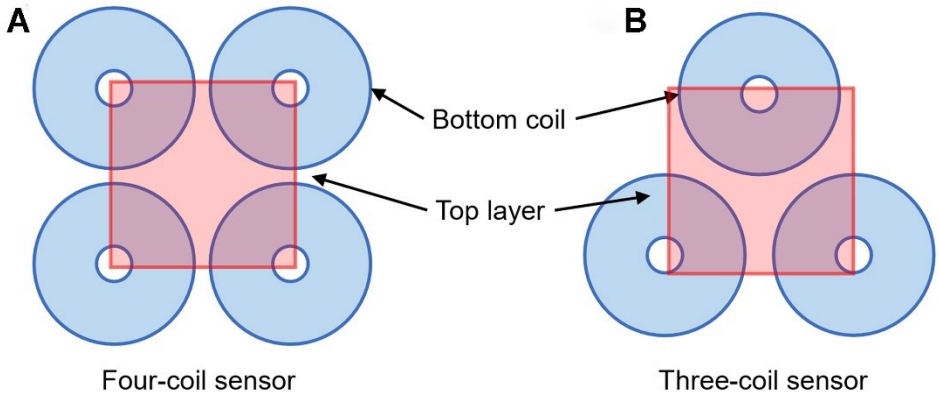

Supplementary Figure 9. Schematic illustrations of tri-axial inductive tactile sensors with different configurations. (A) Sensor consisting of four symmetric sensing coils; (B) sensor consisting of three coils. Both square and circular planar spiral coils can be used for bottom coils. Both square and circular conductive targets can be used for the top layer[5-7,22-24]. Only circular-shaped bottom coil and square-shaped top layer are selected for illustration.

Supplementary Note 9. Calculation of inductance changes along the y-axis with variations in the size and orientation of the top coil.

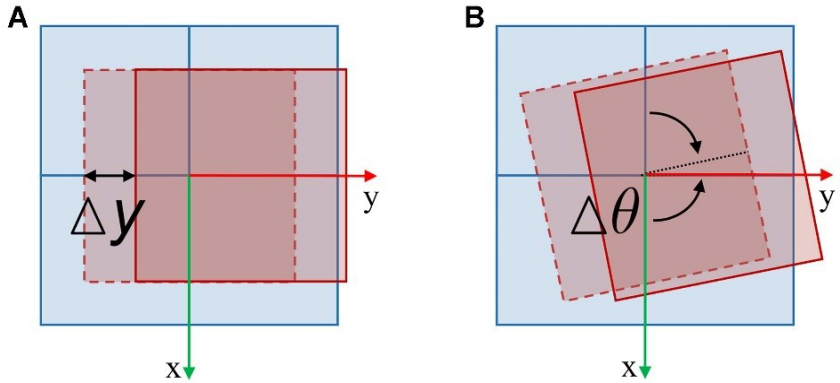

Supplementary Figure 10. Illustration of the (A) lateral movement and (B) orientation of the top coil (red) relative to the bottom coils (blue).

The calculation of inductance changes was performed using MATLAB. Based on the design of the top and bottom coils (Supplementary Figures 7 and 8), the magnetic flux density generated by the coils can be considered uniform. For the lateral movement of the top coil under a shear force, according to Supplementary Equation (3), the calculation of inductance changes was thus based on the changes in overlapping areas between the top and bottom coils. The position of the top coils was defined by their diagonal vertex coordinates (DVC) (Supplementary Figure 10). Considering the coverage ratio and orientation, the initial DVC of the top coil was established. Assuming four bottom coils as a collective unit, the center of this assembly and that of the top coil were made concentric for the initial condition when the force is not applied, as shown in Figure 2A.

The center of the top coil was designated as the origin of the coordinate system. Then the top coil was made to move laterally relative to the bottom coils with a displacement along the *y*-axis ranging from -7 mm to 7 mm, in increments of 0.2 mm. The changes in overlapping areas for each of the four bottom coils were calculated. Therefore, the relationships between inductance changes and lateral movements of the top coil with different coverage ratios and orientations were established.

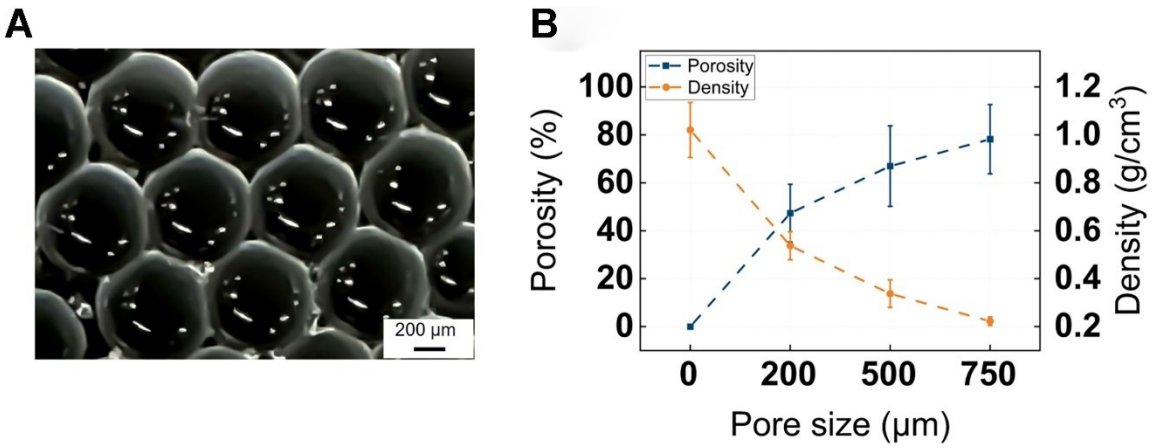

Supplementary Figure 11. Porous compressible layer (PCL) with different pore sizes. (A) Microscopic image of PCL with a pore size of around 700 µm. (B) Porosity and density as a function of pore sizes.

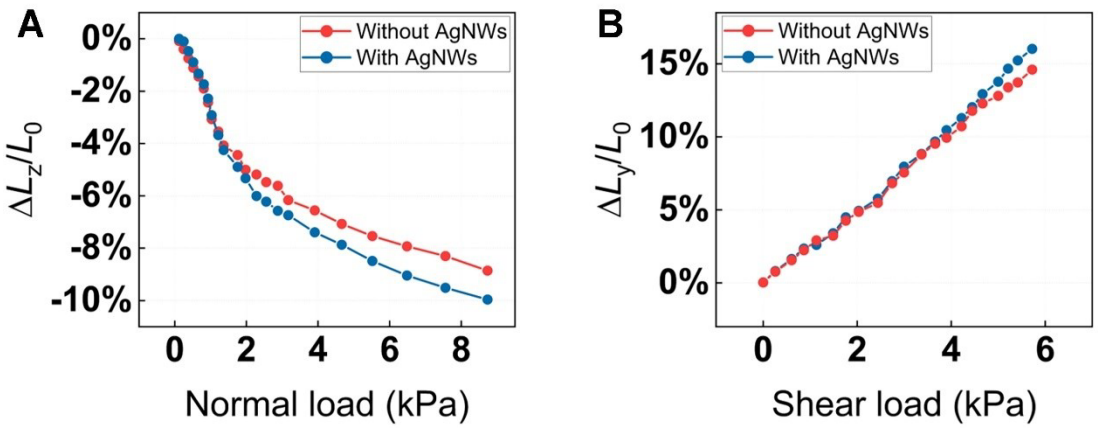

Supplementary Figure 12. (A) Normal and (B) shear sensing performance for sensors based on porous compressible layers with and without AgNWs coating.

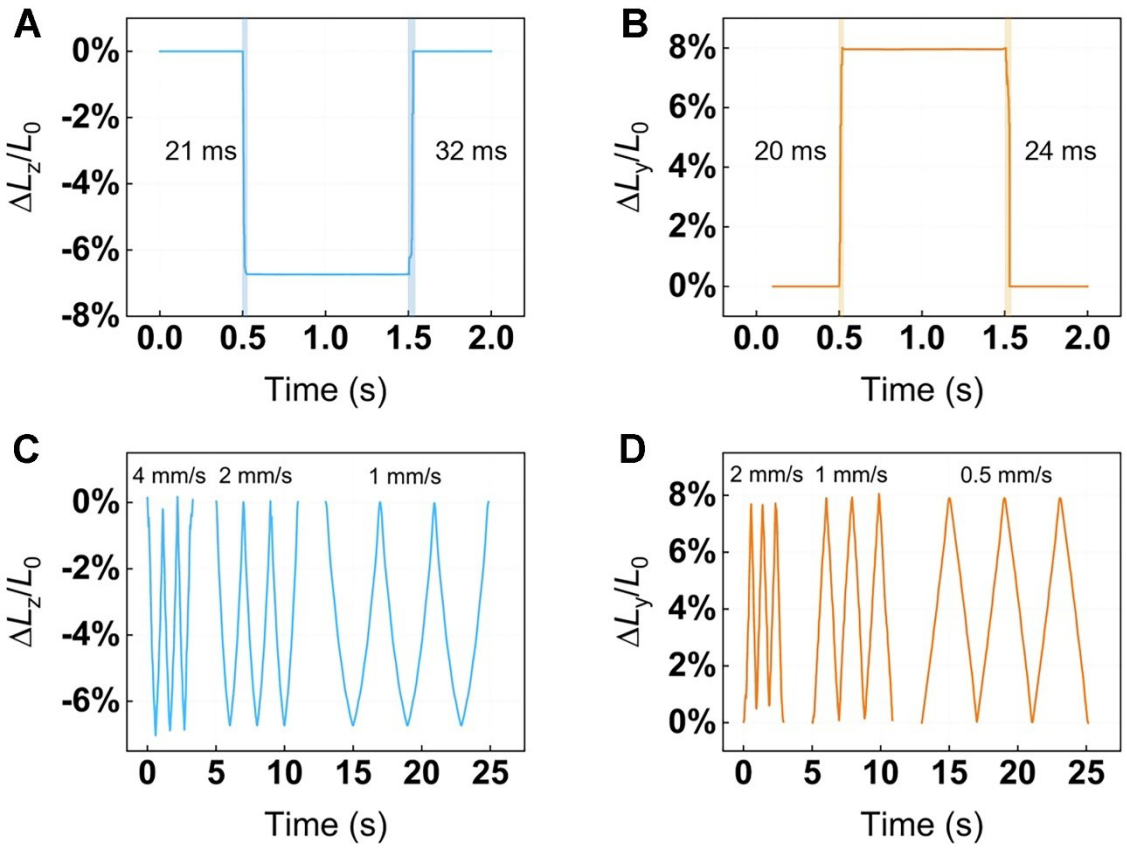

Supplementary Figure 13. Response and recovery time and performance of the dual tri-axial tactile sensors (DTTS) under varying rates of applied loads. Response and recovery time of the DTTS under (A) 3.2 kPa normal loads and (B) 3 kPa shear loads. Inductance changes of (C) 3.2 kPa normal loads and (D) 3 kPa shear loads under varying loading rates, respectively.

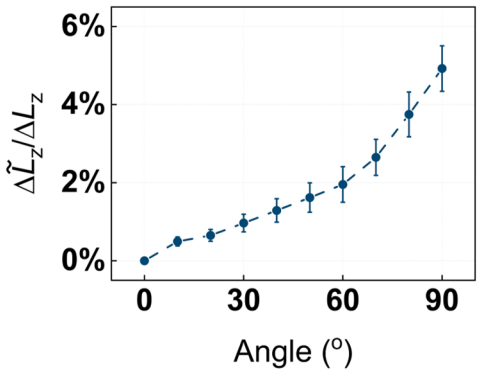

Supplementary Figure 14. Performance of the sensor under bending. ΔL_z represents the inductance change of the sensor at 0° (no bending) when a 0.5 N normal load was applied. $\Delta\tilde{L}_z$ represents the inductance change at different bending angles. When the angle is 0°, $\Delta\tilde{L}_z$ is the same as ΔL_z.

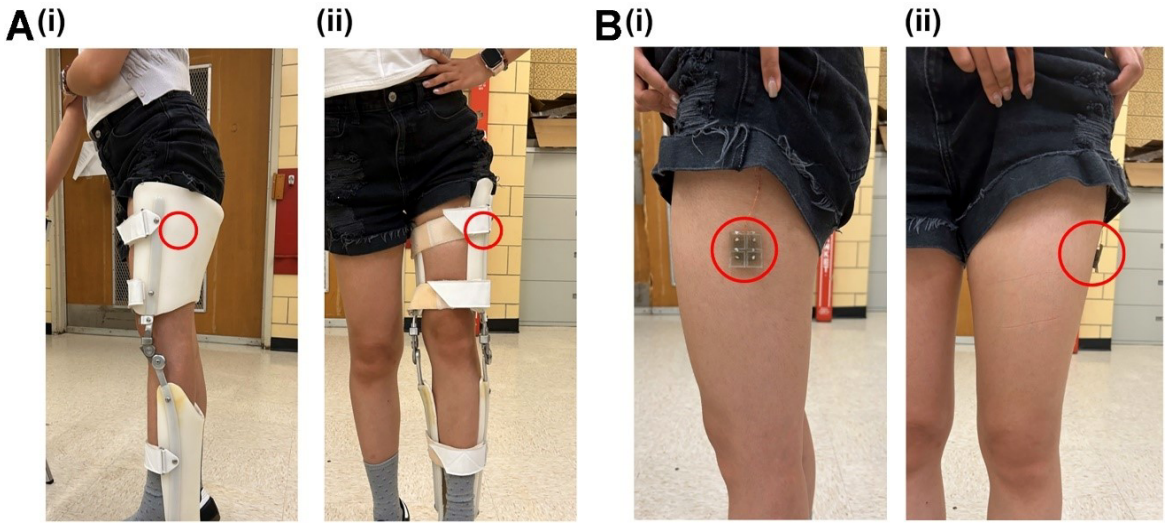

Supplementary Figure 15. Photographs of the sensor attached between the user's upper leg and the thigh cuff of an RGO. (A) Photographs of a user wearing an RGO: (i) Side-view; (ii) front-view. (B) Photographs of the sensor attached to the user's upper leg: (i) Side-view; (ii) front-view. The red circles show the location of the sensor. To facilitate easy attachment, Ecoflex gel was applied on the top and bottom surfaces of the sensor, forming a self-adhesive and biocompatible thin layer[25].

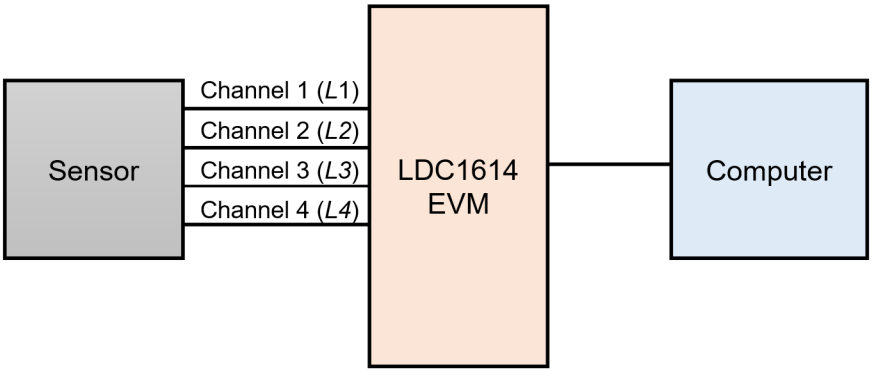

Supplementary Figure 16. Schematic of the system used for demonstrations in real-time tactile sensing between the skin and RGO.

REFERENCES

[1] Kawasetsu, T.; Horii, T.; Ishihara, H.; et al. Size dependency in sensor response of a flexible tactile sensor based on inductance measurement. In *2017 IEEE SENSORS*, Glasgow, UK, October 29-November 1, 2017; IEEE: pp 1-3. DOI: 10.1109/ICSENS.2017.8233908.

[2] Kawasetsu, T.; Horii, T.; Ishihara, H.; et al. Flexible Tri-Axis Tactile Sensor Using Spiral Inductor and Magnetorheological Elastomer. *IEEE Sens. J.* **2018**, *18* (14), 5834-5841. DOI: 10.1109/jsen.2018.2844194.

[3] Ozioko, O.; Hersh, M.; Dahiya, R. Inductance-based flexible pressure sensor for assistive gloves. In *2018 IEEE SENSORS*, New Delhi, India, October 28-31, 2018; IEEE: pp 1-4. DOI: 10.1109/ICSENS.2018.8589826.

[4] Wang, H.; Kow, J.; Raske, N.; et al. Robust and high-performance soft inductive tactile sensors based on the Eddy-current effect. *Sens. Actuators A: Phys.* **2018**, *271*, 44-52. DOI: 10.1016/j.sna.2017.12.060.

[5] Wang, L.; Jones, D.; Chapman, G. J.; et al. An Inductive Force Sensor for In-Shoe Plantar Normal and Shear Load Measurement. *IEEE Sens. J.* **2020**, *20* (22), 13318-13331. DOI: 10.1109/jsen.2020.3006316.

[6] Wang, H.; Jones, D.; de Boer, G.; et al. Design and Characterization of Tri-Axis Soft Inductive Tactile Sensors. *IEEE Sens. J.* **2018**, *18* (19), 7793-7801. DOI: 10.1109/jsen.2018.2845131.

[7] Kawasetsu, T.; Niiyama, R.; Kuniyoshi, Y. Flexible and Soft Inductive Tri-axis Tactile Sensor Using Liquid Metal as Sensing Target. In *2019 IEEE SENSORS*, Montreal, Canada, October 27-30, 2019; IEEE: pp 1-4. DOI: 10.1109/SENSORS43011.2019.8956736.

[8] Wang, H.; Liu, Y.; Li, W.; et al. Design of ultrastable and high resolution eddy-current displacement sensor system. In *IECON 2014-40th Annual Conference of the IEEE Industrial Electronics Society*, Dallas, USA, October 29-November 1, 2014; IEEE: pp 2333-2339. DOI: 10.1109/IECON.2014.7048828.

[9] Peters, C.; Manoli, Y. Inductance calculation of planar multi-layer and multi-wire coils: An analytical approach. *Sens. Actuators A: Phys.* **2008**, *145*, 394-404. DOI: 10.1016/j.sna.2007.11.003.

[10] Rosa, E. B. *The self and mutual inductances of linear conductors*; US Department of Commerce and Labor, Bureau of Standards, 1908.

[11] Yu, L.; Li, S.; Niu, P.; et al. Novel square spiral Coil for achieving uniform Distribution of magnetic Field. In *2019 5th International Conference on Energy, Environment and Materials Science (ICEEMS 2019)*, Singapore, June 21-23, 2019; IOP Publishing: Vol. 332, p 042005. DOI: 10.1088/1755-1315/332/4/042005.

[12] Casanova, J. J.; Low, Z. N.; Lin, J.; et al. Transmitting coil achieving uniform magnetic field distribution for planar wireless power transfer system. In *2009 IEEE Radio and Wireless Symposium*, San Diego, USA, January 18-22, 2009; IEEE: pp 530-533. DOI: 10.1109/RWS.2009.4957405.

[13] Li, S.; Niu, P.; Yu, L.; et al. Design Method of Primary Transmitting Coil for Realizing Large Uniform Magnetic Field Distribution. In *2018 3rd International Conference on Mechanical, Control and Computer Engineering (ICMCCE)*, Huhhot, China, September 14-16, 2018; IEEE: pp 112-116. DOI: 10.1109/icmcce.2018.00030.

[14] Diao, Y.; Shen, Y.; Gao, Y. Design of coil structure achieving uniform magnetic field distribution for wireless charging platform. In *2011 4th International Conference on Power Electronics Systems and Applications*, Hong Kong, China, June 8-10, 2011; IEEE: pp 1-5. DOI: 10.1109/pesa.2011.5982959.

[15] Xu, Q.; Hu, Q.; Wang, H.; et al. Optimal Design of Planar Spiral Coil for Uniform Magnetic Field to Wirelessly Power Position-Free Targets. *IEEE Trans. Magn.* **2021**, *57* (2), 1-9. DOI: 10.1109/tmag.2020.3042131.

[16] Liu, J. Simple technique for measurements of pulsed Gaussian-beam spot sizes. *Opt. Lett.* **1982**, *7* (5), 196-198. DOI: 10.1364/OL.7.000196.

[17] Yao, S.; Yang, J.; Poblete, F. R.; et al. Multifunctional electronic textiles using silver nanowire composites. *ACS Appl. Mater. Interface* **2019**, *11* (34), 31028-31037. DOI: 10.1021/acsami.9b07520.

[18] Hwang, D. J.; Kuk, S.; Wang, Z.; et al. Laser scribing of CIGS thin-film solar cell on flexible substrate. *Appl. Phys. A* **2017**, *123*, 1-11. DOI: https://doi.org/10.1007/s00339-016-0666-7.

[19] Wang, Z.; Kuk, S.; Kim, W. M.; et al. Picosecond laser scribing of bilayer molybdenum thin films on flexible polyimide substrate. *Appl. Surf. Sci.* **2019**, *493*, 320-330. DOI: https://doi.org/10.1016/j.apsusc.2019.06.251.

[20] Jeong, S.; Ham, S. S.; Choi, E. P.; et al. Enhanced mechanical stability of CIGS solar module with Glass/Polyimide/Indium Tin oxide for potentially flexible applications. *ACS Appl. Energy Mater.* **2023**, *6* (7), 3745-3755. DOI: https://doi.org/10.1021/acsaem.2c03957.

[21] *Laser cutting and engraving machine Speedy Series*. Trotec. https://www.troteclaser.com/en-us/laser-machines/laser-engravers-speedy-series (accessed 2024-12-13).

[22] Yeh, S.; Fang, W. Inductive Micro Tri-Axial Tactile Sensor Using a CMOS Chip With a Coil Array. *IEEE Electron Device Lett.* **2019**, *40* (4), 620-623. DOI: 10.1109/led.2019.2901946.

[23] Wattanasarn, S.; Noda, K.; Matsumoto, K.; et al. 3D flexible tactile sensor using electromagnetic induction coils. In *2012 IEEE 25th International Conference on Micro Electro*

Mechanical Systems (MEMS), Paris, France, January 29-February 2, 2012; IEEE: pp 488-491. DOI: 10.1109/MEMSYS.2012.6170230.

[24] Du, L.; Zhu, X.; Zhe, J. An inductive sensor for real-time measurement of plantar normal and shear forces distribution. *IEEE Trans. Biomed. Eng.* **2015**, *62* (5), 1316-1323. DOI: 10.1109/TBME.2014.2386136.

[25] Chen, S.; Yu, L.; Shen, W.; et al. Multimodal 5-DOF Stretchable Electromagnetic Actuators toward Haptic Information Delivery. *Adv. Funct. Mater.* **2024**, *34* (17), 2314515. DOI: 10.1002/adfm.202314515.